



CHALMERS
UNIVERSITY OF TECHNOLOGY

Fluorine-Doped NaTi₂(PO₄)₃ Via Electronic Orbital Modulation and Bandgap Engineering for Aqueous Li/Na/K-Ion Batteries

Downloaded from: <https://research.chalmers.se>, 2025-07-01 19:59 UTC

Citation for the original published paper (version of record):

Xu, T., Yu, J., Ma, J. et al (2025). Fluorine-Doped NaTi₂(PO₄)₃ Via Electronic Orbital Modulation and Bandgap Engineering for Aqueous Li/Na/K-Ion Batteries. Energy and Environmental Materials, In Press.
<http://dx.doi.org/10.1002/eem2.70043>

N.B. When citing this work, cite the original published paper.

Fluorine-Doped $\text{NaTi}_2(\text{PO}_4)_3$ Via Electronic Orbital Modulation and Bandgap Engineering for Aqueous Li/Na/K-Ion Batteries

Tong Xu , Jiaojiao Yu, Junchao Ma, Hongbo Yu, Junling Che, Qixiang Yin, Yukun Xi, Yanyan Cao, Mangmang Shi, Shuting Wang, Wu Wan, Changxin Li, Rui Chen, Jinniu Zhang, Qiyi Zhao, Wei Ren, Mingliang Hu*, and Xifei Li* 

Sodium titanium phosphate ($\text{NaTi}_2(\text{PO}_4)_3$, NTP) has emerged as a promising electrode material due to its three-dimensional open framework. This study investigates the use of NTP in aqueous dilute Li^+/Na^+ electrolytes and extends its application to high-concentration K^+ electrolytes. X-ray photoelectron spectroscopy, X-ray absorption near-edge structure analysis, and density functional theory calculations revealed that highly electronegative fluorine partially substitutes for oxygen in the NTP lattice, resulting in the formation of Ti-F bonds. The substitution effectively modulates the electronic structure of Ti^{4+} , alters the local coordination environment, and influences the redox dynamics. Enhanced long-term cycling stability and rate performance were demonstrated across aqueous sodium-ion, lithium-ion, and potassium-ion half-cells. Among the investigated systems, the aqueous sodium-ion system exhibited the best electrochemical performance, characterized by a single, well-defined charge–discharge plateau, stable cycling behavior with 88.7% capacity retention after 500 cycles at 1 A g^{-1} , and an initial specific discharge capacity of 121.7 mAh g^{-1} at 0.2 A g^{-1} . The results establish F-doped NTP as a promising candidate for advanced energy storage applications in aqueous alkali metal-ion batteries.

1. Introduction

In recent years, the development of advanced energy storage systems has become imperative to meet the escalating demands for high-performance and sustainable battery technologies. In the quest

Dr. T. Xu, J. Yu, J. Ma, H. Yu, Prof. J. Che, Q. Yin, Dr. S. Wang, W. Wan, C. Li, R. Chen, Prof. J. Zhang, Dr. Q. Zhao, Prof. W. Ren, Prof. M. Hu
School of Science, Xi'an University of Posts and Telecommunications, Xi'an 710121, China

E-mail: mlhu0301@163.com

Dr. T. Xu, Dr. Y. Xi, Dr. Y. Cao, Prof. X. Li

Institute of Advanced Electrochemical Energy, School of Materials Science and Engineering, Xi'an University of Technology, Xi'an 710048, China

E-mail: xfli2011@hotmail.com

Dr. M. Shi

Department of Chemistry and Chemical Engineering, Chalmers University of Technology, Kemigården 4, Göteborg SE-412 96, Sweden

 The ORCID identification number(s) for the author(s) of this article can be found under <https://doi.org/10.1002/eem2.70043>.

DOI: 10.1002/eem2.70043

for advanced energy storage systems, aqueous alkali metal-ion batteries have emerged as a promising alternative to traditional non-aqueous counterparts.^[1] These batteries employ water-based electrolytes, offering several advantages over organic electrolytes: 1) safer and less prone to thermal runaway, making them more suitable for large-scale applications; 2) cost-effective and environmentally friendly due to the abundance and low cost of water as a solvent; 3) high ionic conductivity, enabling efficient transport of alkali metal ions during charge and discharge cycles.^[2–4] Among the various alkali metal ions, lithium ion has long been the focus of research and development in battery technologies. However, sodium and potassium ions have gained significant attention due to their abundance, low cost, and similar electrochemical characteristics to Li ions.^[5–7] In aqueous sodium-ion batteries (ASIBs) and aqueous potassium-ion batteries (AKIBs), Na^+ or K^+ serve as charge carriers, shuttling between the cathode and anode during charge and discharge cycles.

Exploring the use of Na and K ions alongside Li ions in aqueous alkali metal-ion batteries holds great research significance, as it can expand the scope of potential applications and contribute to the development of sustainable and scalable energy storage solutions.^[8,9]

$\text{NaTi}_2(\text{PO}_4)_3$ (NTP), a sodium super ionic conductor (NASICON) material with a theoretical capacity of 133 mAh g^{-1} , has garnered significant attention as an anode material for aqueous alkali metal-ion batteries.^[10,11] NTP has a three-dimensional open framework crystal structure, which provides pathways for the diffusion of sodium ions. This unique structure is beneficial for efficient ion diffusion and can contribute to the high-power performance of the battery. While NTP as an anode material for aqueous alkali metal-ion batteries also has some shortcomings that researchers are actively addressing. The main challenges can be summarized as follows:^[12] 1) Poor electrical conductivity caused by the insulating properties of phosphate groups, resulting in a mismatch with ionic conductivity and limiting electrochemical performance. 2) NASICON structures undergo significant volume changes during the insertion

and extraction of sodium ions. 3) The lower reduction potential in aqueous alkali metal-ion electrolytes may lead to hydrogen side reactions, causing degradation of battery performance. To address these issues, researchers have focused on several strategies to improve the performance of NTP. Coating a conductive carbon layer on the NTP particles has the potential to enhance electronic conductivity by offering an additional electron transfer pathway.^[13,14] The core-shell structure also helps alleviate volumetric deformations that occur during the charging and discharging process.^[15] Modified carbon^[16] by doping S, N, and B can generate more active sites, further addressing the electronic-ionic conductivity mismatch issue and boosting the overall electrochemical performance of NTP electrodes. Carbon derivatives^[17–19] like carbon nanofibers, carbon nanotubes, and graphene can form three-dimensional conductive networks, enhancing electron/ion transport kinetics and resulting in outstanding sodium storage properties. Another strategy involves optimizing the morphology and structure of NTP materials,^[17,20–27] which includes reducing the particle size to the nanoscale and designing high-specific-surface structures to shorten the diffusion path of sodium ions and enhance sodium-ion diffusion kinetics. Doping methods mainly include the substitution of titanium (Ti) atoms in NTP and doping of halogen atoms at PO_4^{3-} positions.^[28–30] For example, doping with elements such as Al,^[31] Fe,^[30] Zr,^[32] Sn,^[33,34] Mg,^[35] Mo^[36] and La^[37] can introduce defects or modify the crystal structure, leading to improved electronic conductivity and enhanced ion diffusion. However, these metal dopants often lead to lattice distortion and variations in redox activity, which may impact the long-term structural stability or reduce electrochemical reversibility. Compared with metal-ion doping, F doping follows a unique mechanism. Instead of replacing Ti atoms and directly disrupting the octahedral structure, F influences the bonding characteristics.^[38,39] It induces effects on phosphate groups and forms Ti-F bonds, thereby modulating the local electronic structure of Ti. F doping is expected to provide a more controllable approach to enhancing the stability and functionality of NTP.

Aside from Na^+ ions, NTP with three-dimensional large ionic channels can be also applied in aqueous Li^+ or Li^+/Na^+ hybrid electrolyte.^[40–43] Furthermore, Leonard et al. successfully achieved reversible intercalation of K^+ into/from the $\text{KTi}_2(\text{PO}_4)_3$ anode over a broad voltage range by implementing a “Water-in-Salt” (WIS) system.^[44] Despite significantly restricting the number of water molecules in the solvation sheath, the low K^+ reaction potential could still trigger solvent water electrolysis during long cycle lifetimes. Hence, further research is required to elucidate the influence of F doping on the electronic orbital modulation and bandgap characteristics of NTP anodes in aqueous alkali metal-ion batteries. A deeper understanding of the effects could provide critical insights into optimizing the electrochemical behavior and reaction kinetics of NTP anode for aqueous energy storage applications.

In this study, carbon-coated fluorine-doped sodium titanium phosphate (NTPF) was synthesized via the sol-gel method. The NTPF anode was evaluated in both dilute aqueous Li^+ and Na^+ electrolytes, as well as in an aqueous K^+ WIS electrolyte. The incorporation of fluorine into the NTP structure alters the local electronic environment surrounding Ti atoms and enhances ion transport kinetics. The NTPF anode exhibits favorable electrochemical properties, positioning NTPF as a promising candidate for meeting the performance demands of various aqueous alkali metal-ion batteries.

2. Results and Discussion

2.1. Materials Characterization

To obtain precise phase information of the NTPF samples, X-ray diffraction (XRD) was employed (Figure 1a). The XRD patterns of NTP and NTPF samples were remarkably similar, indicating that fluorine doping does not alter the crystal structure of the parent NTP material, consistent with previous studies.^[29,30,38] Nonetheless, upon F doping, the (113) diffraction peaks in the magnified spectra subtly shift towards larger angles. After F doping in the NTP sample, the crystal plane spacing (d_{hkl}) for the (113) plane decreases, resulting in a corresponding increase in the diffraction angle as per the Bragg diffraction formula. The substitution of fluoride ions induces subtle distortions in the local lattice structure, potentially influencing the electronic structure of adjacent titanium atoms.

The crystal structure disparities between NTP and NTPF were investigated by Rietveld refinement of the XRD patterns (Figure 1b,c). The successful refinement of NTPF revealed a weighted profile R factor (R_{wp}) of 11.54%, indicating good agreement between experimental and calculated data. The crystal structure was indexed to the rhombohedral $R\bar{3}C$ space group (PDF#84-2008), with lattice parameters refined to $a = 8.504 \text{ \AA}$, $b = 8.504 \text{ \AA}$, $c = 21.86 \text{ \AA}$, and a volume of 1369 \AA^3 . The crystalline structure comprises TiO_6 octahedron and PO_4 tetrahedron, forming a 3D NASICON framework characterized by extensive ionic channels facilitating rapid diffusion of alkali metal ions. The observed decrease in lattice parameters is attributed to the small ionic radius of F.

The morphology and element distribution of the prepared NTP and NTPF samples were investigated using scanning electron microscopy (SEM), transmission electron microscopy (TEM), and energy dispersive spectroscopy (EDS) technologies (Figure 1d–j; Figure S1, Supporting Information). The SEM and TEM results unveiled a hierarchical structure within the NTPF materials, where micron-sized particles are intricately constructed from an assembly of nanoscale particles, with individual particle sizes ranging from a minimum of 20 to 50 nm (Figure 1d–g). This multi-level nested structure, characterized by larger micron-sized units composed of smaller nano-sized particles, not only ensures robust stability during cycling but also fosters efficient electrolyte impregnation. By enabling thorough penetration of the electrolyte into the hierarchical pores and channels, this structural arrangement facilitates accelerated alkali metal-ion diffusion. The C-coating layer, with a thickness ranging between 2 and 5 nm, was observed on the surface of the NTPF nanoparticle in Figure 1h. The carbon content of both NTP and NTPF was evaluated using thermogravimetric (TG) analysis. The TG results indicate that the carbon content in NTP and NTPF materials is approximately 3.85% and 4.0%, respectively (Figure S2, Supporting Information). Furthermore, lattice fringes with a spacing of approximately 0.416 nm corresponding to the (113) crystalline plane were observed in NTPF. This observation was aligned with the Rietveld refinements, further validating the structural analysis. Elemental mapping using EDS (Figure 1i,j) confirmed a uniform distribution of Na, Ti, P, O, and F throughout the samples, indicating the successful incorporation of doping elements into the NTPF crystal structure. The chemical compositions of the prepared samples were analyzed using XPS. The XPS spectra of the two samples exhibit characteristic photoelectron peaks corresponding to Na 1s, Ti 2p, P 2p, O 1s, and C 1s, without detectable chemical impurities (Figure 2a). In the Ti 2p spectrum,

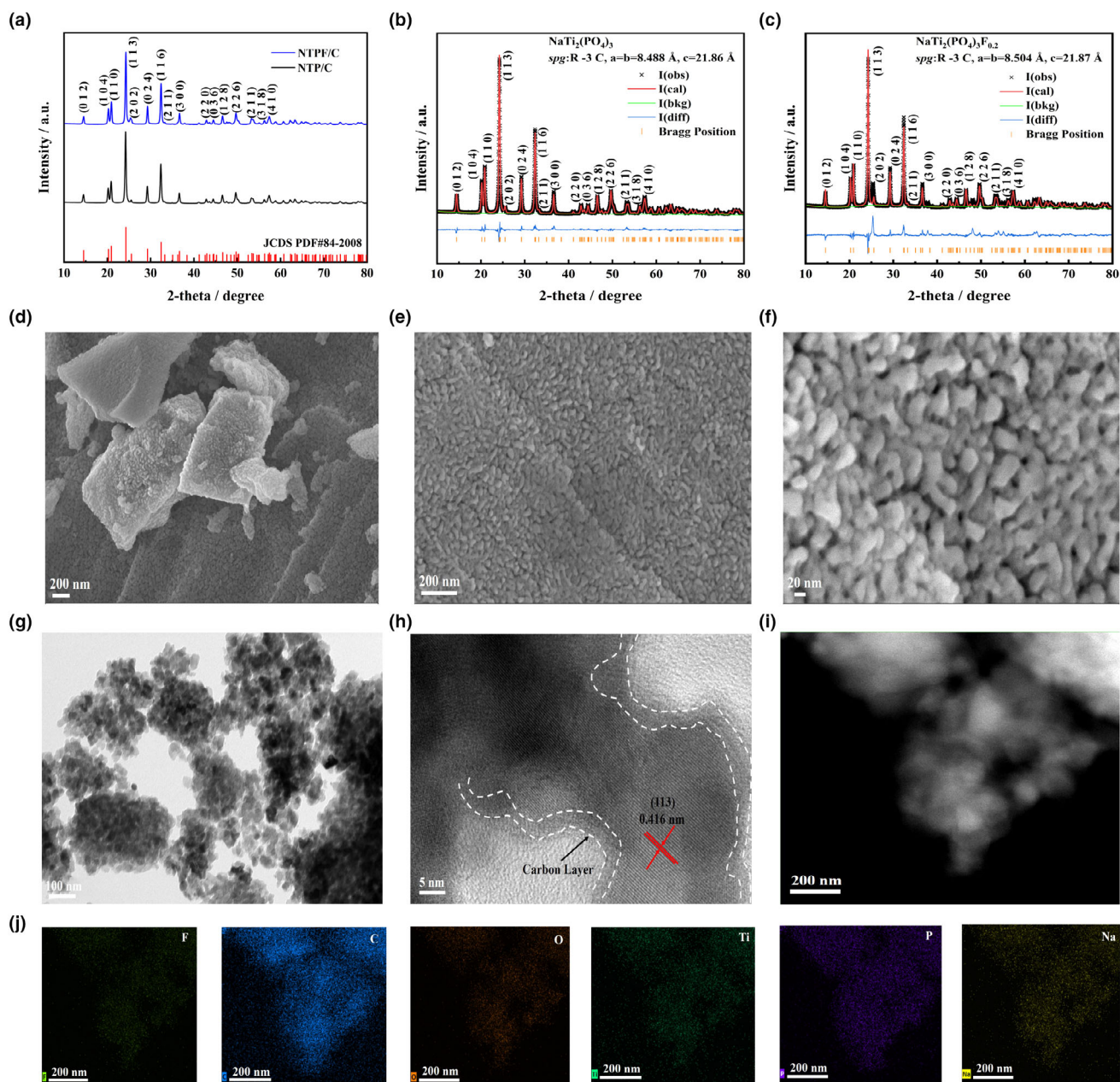


Figure 1. Characterization of NTP/C and NTPF/C: a) XRD patterns of NTP/C and NTPF/C; b) Refinement of NTP; c) Refinement of NTPF; d–f) SEM images of NTPF/C; g) h) TEM and HRTEM images of NTPF/C; i, j) EDS mapping of NTPF/C.

the peaks observed at 465.3 and 469.3 eV represent Ti 2p_{1/2} and Ti 2p_{3/2}, respectively, indicating the prevalence of Ti⁴⁺ state. Two minor peaks appearing at 463.0 and 458.1 eV signify the existence of Ti³⁺ (Figure 2b). According to the charge compensation mechanism, these changes can significantly affect the electronic structure of Ti by changing the electronic structure and local electronic state. Notably, the NTPF sample also exhibits two resolved peaks of F 1s at 686.8 and 685.0 eV, attributed to C-F and Ti-F bonds, respectively (Figure 2c). Semi-quantitative analysis performed using Avantage software indicates that the atomic percentage of fluorine is

approximately 0.53% (Table S1, Supporting Information), suggesting a low-level but effective F doping in the NTP framework.

Fluoride ion doping modifies the nature of Ti-O bonds by introducing Ti-F bonds, which differ in bond length and strength from Ti-O bonds. This substitution alters the local coordination environment of titanium, resulting in changes to its electronic structure. The C 1s spectra of the NTPF samples exhibit three distinctive peaks at 289.3, 286.3, and 284.7 eV (Figure 2d), corresponding to the C-F, C-O, and C-C bonds, respectively. Integration of XPS spectra reveals that F is not solely doped into the NTP lattice but is also in situ incorporated into the

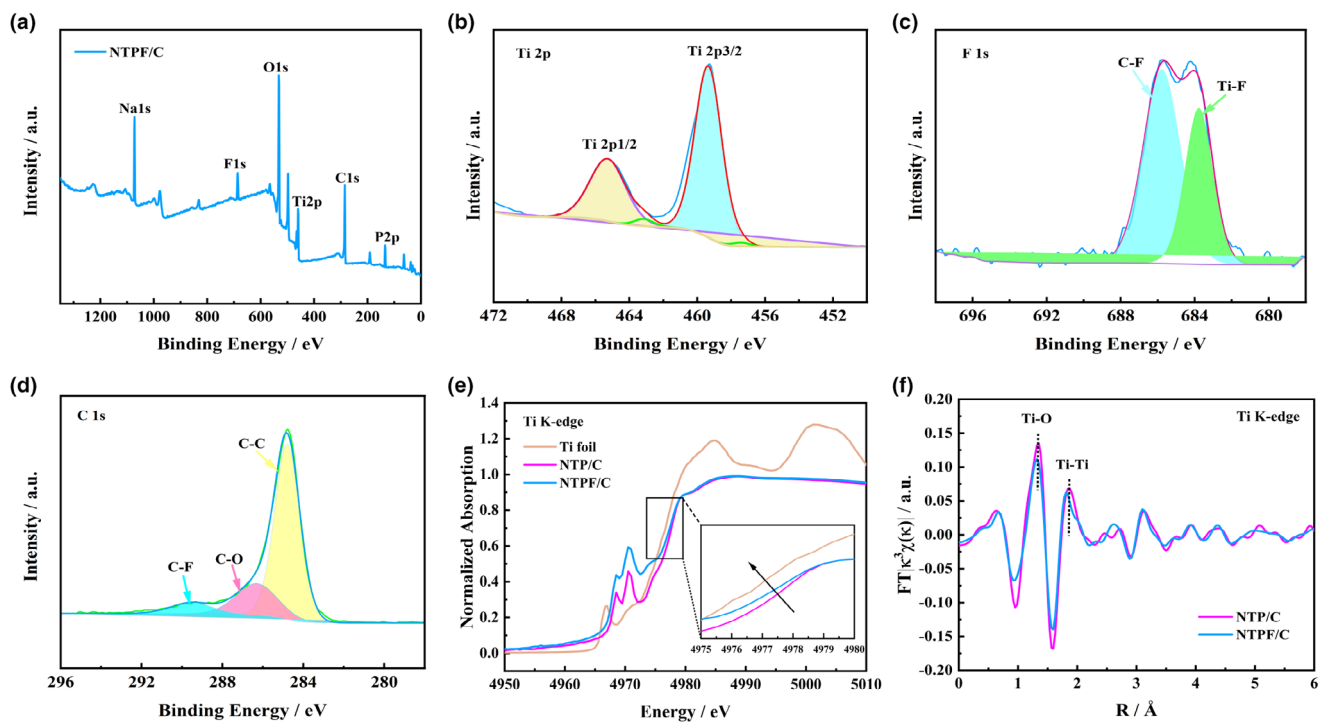


Figure 2. a) XPS spectra of NTPF/C; b) Ti 2p spectrum; c) F 1s spectrum; d) C 1s spectrum; e) Ti K-edge XANES patterns; f) Fourier-transformed Fourier transforms of Ti K-edge EXAFS patterns. NTPF anode in ASIBs.

carbon matrix.^[45,46] The defects formed on the carbon surface serve as additional active reaction sites, facilitating the accelerated diffusion of alkali metal ions.^[28] Fluorine ions doped into the sodium titanium phosphate lattice form Ti-F bonds with titanium atoms. This bonding alters the distribution of the electron cloud around the titanium ions, thereby affecting their local electronic structure.

Synchrotron X-ray absorption near-edge structure (XANES) analysis was employed to further investigate the properties of NTP and NTPF samples. XANES spectra (Figure 2e) revealed a triple pre-edge feature preceding the main absorption peak in both samples, attributed to the distorted configuration of TiO₆ units within the crystal structure.^[47] The absorption edge shifted towards lower energies in NTPF, closer to that of metallic Ti foil, suggesting a reduction in the titanium valence state induced by fluorine doping. F doping induces a redistribution of charge, leading to a new equilibrium state. This adjustment in charge distribution further influences the valence state and local electronic configuration of titanium ions. This finding was corroborated by XPS, which provided consistent results with the XANES observations. Moreover, extended X-ray absorption fine structure (EXAFS) analysis at the Ti K-edge further elucidated the structural details. R-space plots (Figure 2f) exhibited two prominent peaks corresponding to Ti-O and Ti-Ti bond positions, offering atomic-level insights into the local coordination environment of titanium atoms within the samples. Remarkably, fluorine doping resulted in a shift of the Ti-O bond length from 1.34 Å in NTP to 1.31 Å in NTPF. Similarly, the Ti-Ti bond length shifted from 1.85 Å in NTP to 1.81 Å in NTPF. The concurrent shortening of both Ti-O and Ti-Ti bonds following fluorine doping suggests a potential enhancement in electron transfer during the charge-discharge process. Fluorine doping in the NASICON-type NTP structure induces

modifications in the Ti bonding characteristics and charge balance. The partial reduction of Ti⁴⁺ leads to the formation of a mixed-valence state structure. Consequently, the chemical formula of F-doped NTP can be expressed as NaTi_{2-y}⁴⁺Ti_y³⁺(PO₄)_{3-x}F_x (NaTi₂(PO₄)_{3-x}F_x), where *y* represents the proportion of reduced Ti³⁺, and *x* denotes the extent of F substitution for PO₄³⁻ groups.

UV-vis diffuse reflectance spectroscopy (UV-vis DRS) was employed to determine the band gaps of NTP and NTPF samples (Figure S3a,b, Supporting Information). The optical band gaps were deduced using Tauc plots as follows:

$$(\alpha h\nu)^{1/n} = A(h\nu - E_g) \quad (1)$$

where α represents the absorption index, h is Planck's constant, ν is the frequency, E_g is the bandgap, and $n = 1/2$ was used. The undoped NTP exhibited a band gap of approximately 3.48 eV, while the fluorine-doped NTPF showed a reduced band gap of about 3.39 eV. The reduction in the band gap due to F doping suggests a decrease in electronic transition resistance, enhancing the electrochemical performance of the anode material. To further assess the impact of F doping on electronic conductivity, the four-point probe method was utilized (Figure S4, Supporting Information). The average electronic conductivity was measured to be 11.21 $\mu\text{S cm}^{-1}$ for NTP and 14.75 $\mu\text{S cm}^{-1}$ for NTPF. This observation confirms the expectation that F doping in the NTP lattice induces an electronic modulation effect on the phosphate group. Therefore, we can anticipate that the electrochemical performance of the NTP electrode in aqueous alkali metal-ion batteries will be enhanced with the addition of doped F elements.

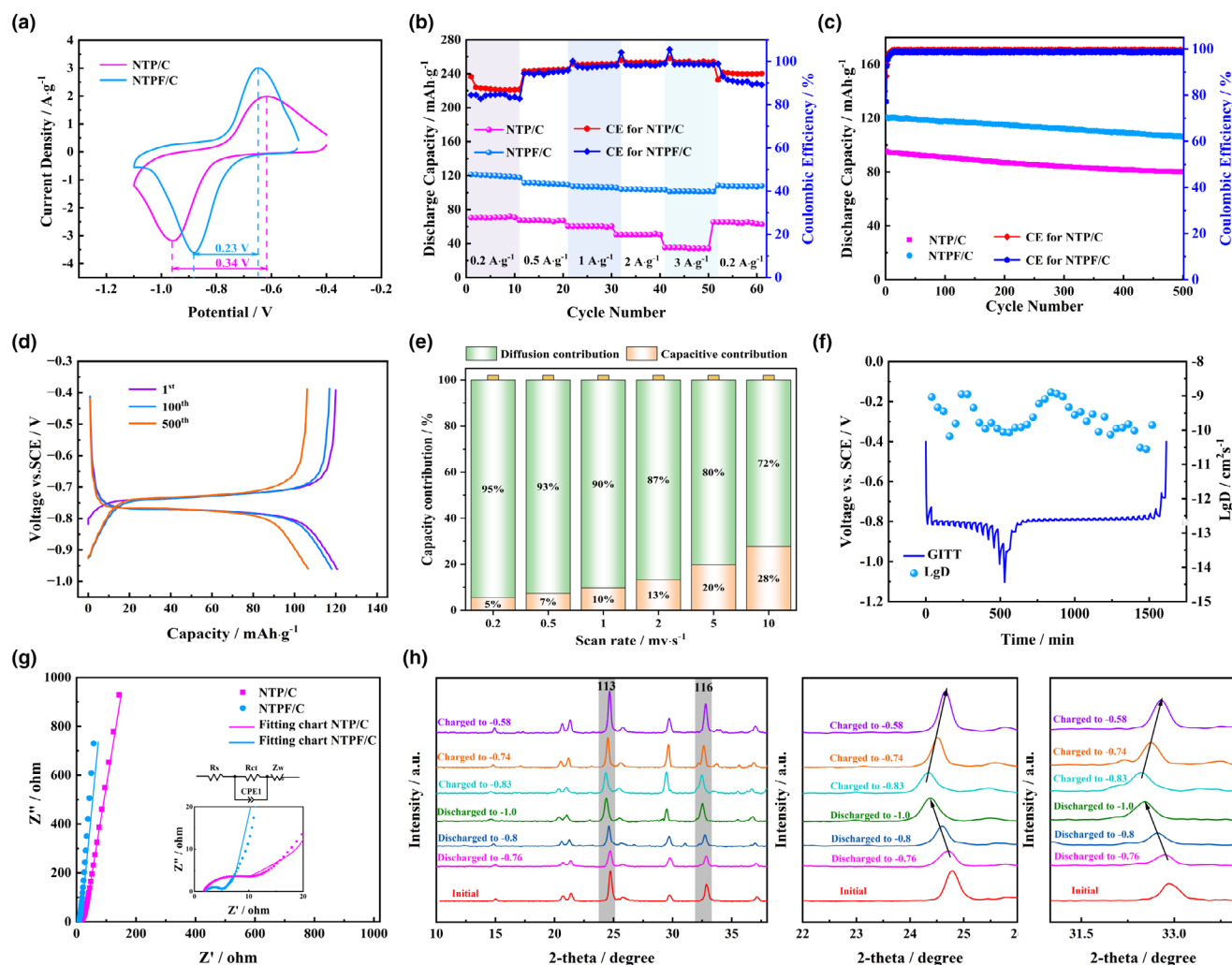


Figure 3. ASIBs in 5 M NaNO₃: a) Comparison of 2 mV s⁻¹ for NTP/C and NTPF/C; b) Rate performance of NTP/C and NTPF/C composites; c) Cycling stability of NTP/C and NTPF/C composites; d) Charge/discharge curves at 1st, 100th, and 500th for NTPF/C; e) Histogram of capacitance contribution; f) Voltage curves for the GITT test and the LgDNA+ of NTPF; g) EIS of NTP/C and NTPF/C composites and equivalent circuit used for EIS fitting; h) Ex situ X-ray diffraction of NTPF/C electrode in ASIBs for initial, different discharge and charge states.

2.2. NTPF Anode in ASIBs

Considering the primary application of NTP anodes in ASIBs, we commenced by investigating the electrochemical properties of both NTP and NTPF in a 5 M NaNO₃ aqueous electrolyte. **Figure 3b** illustrates the rate performances of the two samples. Initially, at a low current density of 0.2 A g⁻¹, the specific discharge capacities of the NTP anode (70.6 mA h g⁻¹) were lower than those of the NTPF (121.7 mA h g⁻¹). As the current density escalated from 0.2 to 3 A g⁻¹, the advantages of the specific discharge capacity of the F-doped samples gradually became evident. At a current density of 3 A g⁻¹, the disparity in specific discharge capacities between the two anodes peaked. Specifically, the specific discharge capacities of the NTP and NTPF anode were 35.4 and 101.1 mA h g⁻¹, respectively. It is noted that the coulombic efficiency was relatively low at low current densities. This phenomenon can be attributed to the occurrence of hydrogen evolution reactions (HER) at

the electrode–electrolyte interface under low current conditions. Due to the inherently narrow electrochemical stability window of aqueous electrolytes, the anode potential at low current density more easily reaches the threshold for HER. Meanwhile, the sluggish kinetics at low current further exacerbate the side reactions, thereby reducing the overall coulombic efficiency. **Figure S5a,b**, Supporting Information display the charge/discharge profiles of two anodes prepared under current densities ranging from 0.2 to 3 A g⁻¹ (with a voltage range of -0.95 to -0.4 V vs SCE). The specific discharge capacities of the NTP and NTPF electrodes were 70.6, 67.4, 60.4, 50.5, and 35.4 mA h g⁻¹ and 121.7, 111.6, 107.5, 104.2, and 101.1 mA h g⁻¹, respectively. Both samples exhibit distinct charge–discharge plateaus in their curves. The slight improvement in specific capacity, particularly evident at higher current densities, with the incorporation of F elements, underscores the method's efficacy in enhancing electrochemical performance. The long-term cycling stabilities of the two samples were evaluated in **Figure 3c**.

After 500 cycles at 1 A g^{-1} , the capacity retentions of the NTP and NTPF anode were 83.9% and 88.7%, respectively. The formation of Ti-F bonds, which are generally stronger than Ti-O bonds, can enhance the stability of the Ti sites within the NTP structure. This stronger bonding can improve the structural integrity of the material during the redox process, reducing the likelihood of lattice distortion or degradation. Figure S5c, Supporting Information and Figure 3d depict the charge/discharge curves of NTP and NTPF anode materials at a current density of 1 A g^{-1} for the 1st, 100th, and 500th cycles, respectively. Both sets of curves exhibit stable charge/discharge voltage plateaus. Notably, the potential difference between the charging and discharging curves of the NTPF anode material remains consistent under identical current densities, indicative of its stable charge and discharge process.

Figure S6a,b, Supporting Information present the CV curves of NTP and NTPF electrodes at different scanning rates from 0.2 – 10 mV s^{-1} . Along with a pair of well-defined redox peaks appearing for each curve of the NTPF anode. These represent the $\text{Ti}^{4+}/\text{Ti}^{3+}$ redox couple when sodium-ion insertion/extraction occurs. While for the NTP anode, the polarization phenomenon was magnified during rapid scanning, particularly at scanning rates of 5 and 10 mV s^{-1} . Reduction peaks were not fully manifested, even at a low potential of -1.2 V versus SCE, heightening the risk of triggering hydrogen evolution side reactions. The polarization of both materials, NTP and NTPF, becomes more apparent in the comparative CV curves at 2 mV s^{-1} in Figure 3a. The potential difference corresponding to the peak current density of the anode material decreases by 0.23 V from 0.34 V after fluorine doping. Additionally, NTPF exhibits a higher peak current intensity compared to NTP, suggesting lower polarization and greater electrochemical activity in the redox process. The slope values (b) can be obtained through linear fitting with $\log i$ and $\log v$. The calculated b -values for the oxidation peaks of NTP and NTPF are 0.74 and 0.57 , respectively (Figure S26c,d, Supporting Information), indicating that diffusion control continues to dominate the battery behavior after F doping. It is impossible to unequivocally determine the proportion of capacitance and diffusion control by comparing the values of b . Therefore, the exact percentage of capacitive contribution and diffusion control was quantified using the following equation:

$$i(v) = k_1 v + k_2 v^{1/2} \quad (2)$$

At a specified potential (v), the current density response (i_p) can be depicted as the amalgamation of capacitive effects ($k_1 v$) and diffusion-controlled reactions ($k_2 v^{0.5}$). The determination of k_1 and k_2 constants can be achieved by analyzing CV currents at various current scan rates. By discerning these constants, it becomes feasible to distinguish the proportion of current stemming from surface capacitance and diffusion-controlled processes. As shown in Figure 3e, the diffusion-controlled contribution gradually decreases from 95% to 72% as the scan rate increases from 0.2 to 10 mV s^{-1} . At lower scan rates (0.2 – 1 mV s^{-1}), the charge storage process is predominantly governed by ion diffusion, indicating efficient Na^+ intercalation/de-intercalation within the electrode material. As the scan rate increases (2 – 5 mV s^{-1}), the diffusion-controlled contribution declines slightly (87–80%), suggesting the emergence of capacitive behavior due to surface or near-surface charge storage.

The ionic diffusion coefficients of NTP and NTPF were evaluated using Galvanostatic Intermittent Titration Technique (GITT). The calculation formula is as follows:^[48]

$$D = \frac{4}{\pi\tau} \left(\frac{m_B V_M}{M_B S} \right)^2 \left(\frac{\Delta E_s}{\Delta E_\tau} \right) \quad (3)$$

V_M —Molar volume of the material; M_B —Relative molecular mass of the material; m_B —Mass of the material; S —Surface area of the material; ΔE_s —Change in steady-state voltage; ΔE —the change in cell voltage during the current pulse, we derive the sodium ion diffusion coefficients of the anode materials (Figure 3f and Figure S7, Supporting Information). In ASIBs, the calculated results of NTPF are $3.515 \times 10^{-10} \text{ cm}^2 \text{ s}^{-1}$ and NTP are found to be $3.575 \times 10^{-11} \text{ cm}^2 \text{ s}^{-1}$, respectively. This faster diffusion kinetics augments the sodium-ion transport characteristics of the electrode material in ASIBs anode materials, thereby enhancing its high-rate performance. To delve deeper into the reaction kinetics of the NTP and NTPF samples, electrochemical impedance spectra were gathered (Figure 3g). Each Nyquist curve exhibits a semicircle in the high-frequency region and a sloping line in the low-frequency region, enabling the determination of charge transfer resistance (R_{ct}), electrolyte impedance (R_s), and Warburg impedance (Z_w). The inset in Figure 3g shows the equivalent circuit diagram used for impedance fitting. The calculated impedance parameters are detailed in Table S2, Supporting Information. The R_{ct} value for NTPF (3.10Ω) is lower than that of NTP (11.45Ω), indicating a more favorable scenario for reducing kinetic confinement. The results show a notable reduction in charge transfer resistance and faster Na^+ diffusion in the F-doped NTP compared to pristine NTP, confirming that F doping enhances ion mobility and accelerates the intercalation process. Furthermore, the coefficient of Z_w for NTPF (16.37Ω) is lower than that of NTP (27.28Ω), suggesting an enhancement of charge transfer within the F-doped anode electrode.

As depicted in Figure 3h, to gain further insights into the structural evolution of NTPF during desodiation and sodiation, ex situ XRD measurements were conducted under various charging and discharging states. These measurements illustrated the shifting pattern of characteristic diffraction peaks corresponding to different diffraction angles alongside the charging and discharging curves of the NTPF anode. Initially, the diffraction peaks located at 24.78° and 32.91° , corresponding to the (113) and (116) planes respectively, shifted towards lower 2θ angles during the discharge process, followed by a reversal of this trend during charging. This variation in peak positions reflects the increase/decrease of the interlayer distance caused by the insertion/extraction of Na^+ ions in the electrode. A weak peak near the (116) position appears during the charging process of the NTPF electrode, which is attributed to the formation of a new phase, $\text{Na}_3\text{Ti}_2(\text{PO}_4)_{3-x}\text{F}_{3x}$, during sodiation. Upon desodiation, this newly emerged peak gradually diminishes and eventually aligns with the original NTPF phase peaks, indicating a reversible phase transition.

2.3. NTPF Anode in ALIBs

In Figure 4b, the performance of the two samples is compared across current densities ranging from 0.1 to 2 A g^{-1} . Throughout all tested

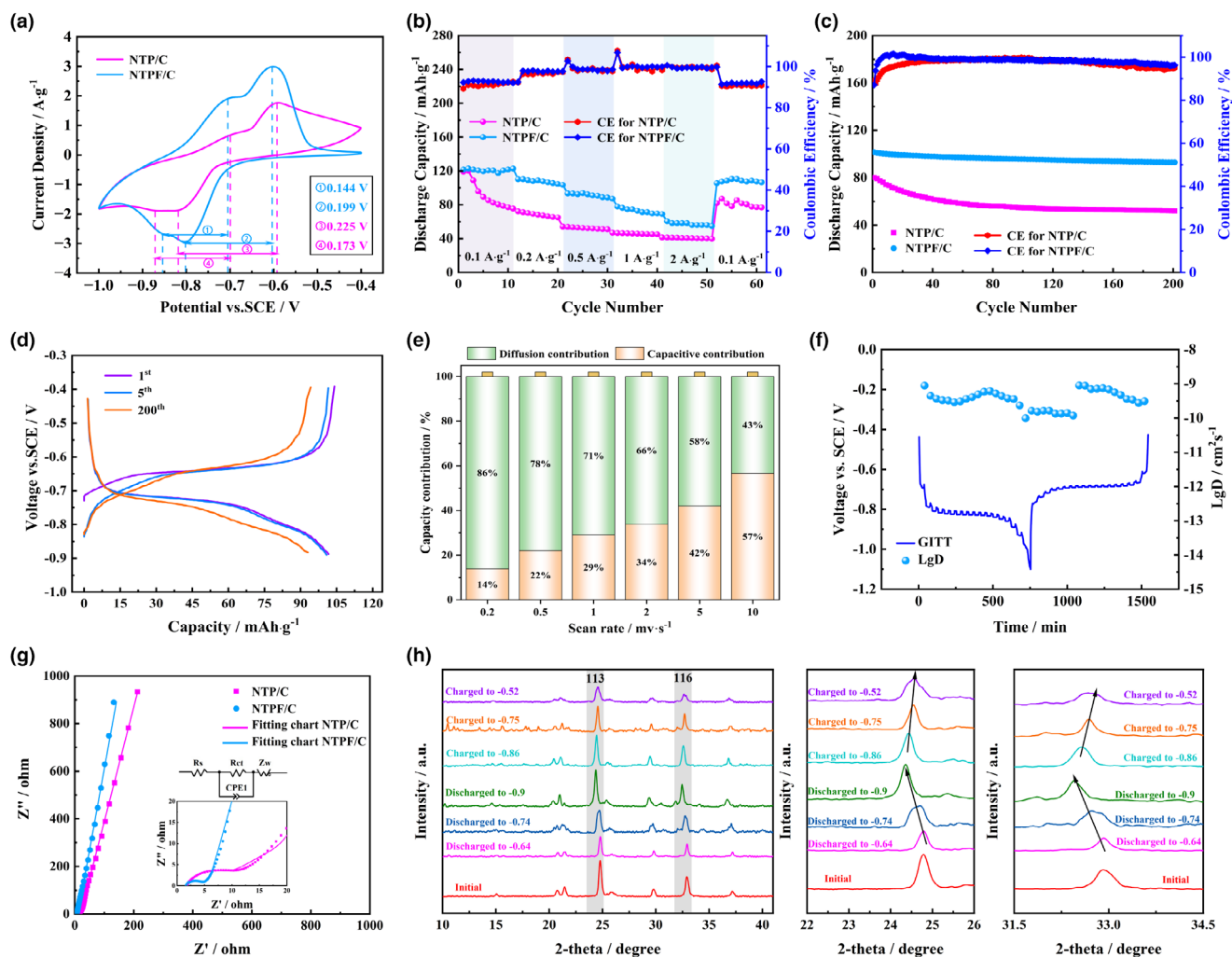


Figure 4. ALIBs in 5 M LiNO₃: a) Comparison of 2 mV s⁻¹ for NTP/C and NTPF/C; b) Rate performance of NTP/C and NTPF/C composites; c) Cycling stability of NTP/C and NTPF/C composites; d) Charge/discharge curves of NTPF/C at a current density of 1 A g⁻¹; e) Histogram of capacitance contribution; f) Voltage curves for the GITT test and the LgDLi⁺ of NTPF; g) EIS of NTP/C and NTPF/C composites and equivalent circuit used for EIS fitting; h) Ex situ X-ray diffraction of NTPF/C electrode in ALIBs for initial, different discharge and charge states.

current densities, the NTPF anode electrode exhibits superior discharge capacity compared to the NTP anode. Furthermore, the advantage in specific discharge capacity of the F-doped samples becomes increasingly pronounced as the current density escalates from 0.1 to 2 A g⁻¹. This underscores the effectiveness of employing a suitable doping strategy in enhancing the charge/discharge performance of NTP under high current densities in ALIBs. Figure 4c illustrates the cycling performance of the two samples in ALIBs. After 200 cycles at 1 A g⁻¹, the capacity retention rates for the NTP and NTPF anodes are 64.8% and 91.6%, respectively. Figure S8, Supporting Information and Figure 4d show the charge/discharge curves of the NTP and NTPF anode materials at the 1st, 5th, and 200th cycles at a current density of 1 A g⁻¹, respectively. Both sets of curves exhibit stable charge/discharge voltage plateaus. The potential difference between the charge/discharge curves of the NTPF anode material is smaller at the same current density than for the NTP anode, suggesting reduced electrode polarization and enhanced stability during the charge/discharge process.

The CV curves of NTP and NTPF at varying scan rates (0.2–10 mV s⁻¹) in Figure S9a,b, Supporting Information reveal two symmetrical pairs of oxidation–reduction peaks, mirroring the charge–discharge curves and maintaining consistent shapes. The NASICON-type structure of NTP features two distinct M1 and M2 sites. In the initial NTP structure, Na⁺ ions predominantly occupy the M1 site. Upon the first lithium-ion intercalation, the peak at -0.7 V vs. SCE corresponds to the occupation of the M2 site by lithium ions. As the potential increases, more Li⁺ intercalates, leading to the transformation of the NTP phase into the Li₂NaTi₂(PO₄)₃ phase. In the Li₂NaTi₂(PO₄)₃ structure, the M1 and M2 sites are disrupted, forming M3 sites that are distinct from M1 and M2.^[43,49] Further Li⁺ intercalation occurs into the M3 sites, manifesting as a reversible peak at -0.8 V versus SCE. Figure 4a presents a comparison of the CV curves for NTP and NTPF. The observed reduction in the hysteresis of the two pairs of redox peak potentials, from 0.173 to 0.144 V and from 0.225 to 0.199 V, highlights the enhanced electrochemical kinetics resulting from F doping.

Additionally, the calculation of b -values corresponding to the oxidation and reduction peaks at various scan rates is shown in Figure S9c,d, Supporting Information. These values suggest a blend of surface-controlled and diffusion-controlled mechanisms in ALIBs for both anode materials. The diffusion-controlled contribution decreases from 86% at 0.2 mV s^{-1} to 43% at 10 mV s^{-1} for NTPF in ALIBs (Figure 4e), which is notably lower than that observed in ASIBs. At lower scan rates ($0.2\text{--}1 \text{ mV s}^{-1}$), the diffusion-controlled contribution remains relatively high (86–71%), implying that Li^+ intercalation is still the primary charge storage mechanism. However, as the scan rate increases ($2\text{--}10 \text{ mV s}^{-1}$), the diffusion-controlled contribution declines more significantly (66–43%), with a substantial increase in the capacitive-controlled process. According to GITT calculation, in 5 M LiNO_3 aqueous electrolyte, the lithium-ion diffusion coefficient of NTPF is $4.096 \times 10^{-10} \text{ cm}^2 \text{ s}^{-1}$ and the lithium-ion diffusion coefficient of NTP is $4.025 \times 10^{-10} \text{ cm}^2 \text{ s}^{-1}$ (Figure 4f and Figure S10, Supporting Information). The enhanced diffusion of Li^+ ions is attributed to the creation of ion pathways by F doping, which facilitates faster ion extraction and insertion within the electrode material. In contrast to ASIBs, NTPF demonstrates reduced electrochemical impedance in ALIBs (Figure 4g, Table S3, Supporting Information). This difference could stem from the smaller ionic radius and mass of Li^+ compared to Na^+ . However, when considering reversible specific capacity and cycling stability, NTPF in the ALIBs system does not exhibit performance on par with that in the ASIBs system. This suggests that NTPF is better suited for and more compatible with the aqueous sodium-ion battery system.

Ex situ XRD analyses were conducted to explore the energy storage mechanism of the NTPF electrodes in the ALIBs. Figure 4h illustrates the XRD patterns of the NTPF electrodes at the initial stage, various discharging stages, and different charging stages after three cycles of 0.1 A g^{-1} . The peaks, such as (113) and (116), undergo a shift towards lower 2θ values during Li^+ insertion, returning to their initial positions during Na^+ extraction. An expansion of the lattice occurs during discharge, followed by a reversible contraction during charging. It is worth noting that splitting and re-organization of diffraction peaks were observed at both lower diffraction angles and near the (116) plane during the Li-intercalation process. This indicates that the new phase ($\text{Li}_2\text{NaTi}_2(\text{PO}_4)_3\text{-xF}_x$) formed during the lithiation process. During the de-intercalation process, the newly emerged peaks gradually weakened and eventually disappeared, indicating a reversible transformation back to NTPF phase. Moreover, Na^+ preferentially occupies the M1 site of NTP and exhibits a stronger affinity for this site compared to lithium ions Li^+ .^[49,50] Consequently, the cycling process primarily involves the intercalation of Li^+ at the NTPF electrode and almost no Na^+ leaching during this process in ALIBs.

2.4. NTPF Anode in WIS AKIBs

The electrolyte choice for AKIBs initially favored KNO_3 due to its shared anion with ASIBs and ALIBs electrolytes (NaNO_3 and LiNO_3). However, even at its saturated concentration, only one oxidation peak appeared in the CV curve (Figure S11, Supporting Information). There was no discernible reduction peak symmetrically linked to it. The noticeable dip in the curve at a potential as low as -1.2 V corresponded to the side reaction of hydrogen precipitation within this low-concentration aqueous electrolyte. Hence, we proceeded to employ 31 m KAc to establish a WIS system, aimed at expanding the voltage window of the aqueous electrolyte.^[51] We also conducted CV tests

using a diluted salt concentration of 1 M KAc for comparison. The results revealed that only in the 31 m KAc WIS aqueous electrolyte did a distinct redox peak emerge, exhibiting superior symmetry compared to the diluted counterpart. This observation indicates that the NTPF anode within the AKIBs, composed of this WIS electrolyte, exhibits enhanced reversibility. Based on this, we proceeded to examine the electrochemical characteristics of both NTP and NTPF samples within AKIBs, utilizing a 31 m KAc WIS electrolyte.

Comparing the rate performance of NTP and NTPF in AKIBs (Figure 5b) reveals that the NTPF anode delivers a higher capacity of 52.6 mAh g^{-1} at a current density of 0.05 A g^{-1} and maintains 63.1% at 1 A g^{-1} of its initial capacity. In contrast, the NTP anode achieves a relatively lower capacity (45.5 mAh g^{-1}) and retains only 46.4%. F doping facilitates the enhancement of both the rate capability and specific capacity of the NTP anode in AKIBs. The cycling stability of NTP and NTPF was examined in a 31 m KAc WIS electrolyte at 1 A g^{-1} (Figure 5c). The discharge capacities of NTPF and NTP samples decline from 71.1 to 35.3 mAh g^{-1} and 43.6 to 24.5 mAh g^{-1} , respectively, over the initial 300 cycles. Interestingly, from cycles 300 to 1000, the discharge capacities begin to increase, reaching 38.3 mAh g^{-1} for NTPF and 25.1 mAh g^{-1} for NTP. By stabilizing the electronic structure of Ti and improving the bonding strength, fluoride ion doping can reduce capacity fading over multiple cycles, thereby enhancing the long-term cycling stability of NTP in AKIBs. The electrochemical performance of both NTP and NTPF anodes was further evaluated through galvanostatic charge/discharge curves at 1 A g^{-1} cycling across different cycles (Figure S12, Supporting Information and Figure 5d). Both materials exhibited significant charge/discharge plateaus corresponding to the equilibrium voltage of $\text{Ti}^{4+}/\text{Ti}^{3+}$. Notably, the NTPF anode demonstrated a longer charging/discharging plateau and lower voltage hysteresis compared to the NTP electrode at the same number of cycles. Even after 1000 cycles, NTPF still exhibited a more pronounced charging/discharging plateau, indicating that the F-doped NTP possesses faster kinetics and a stable structure capable of accommodating potassium-ion intercalation.

The CV curves of NTP and NTPF with different scan rates ($0.2\text{--}10 \text{ mV s}^{-1}$) in Figure S13a,b, Supporting Information clearly display symmetric oxidation–reduction peaks and maintain the same shape, indicating a highly reversible electrochemical reaction of both samples in the AKIBs WIS system. The CV curves of NTP and NTPF are compared in Figure 5a. The CV area of the NTPF electrode is larger, and the potential difference corresponding to the peak current density of the two electrodes is mainly reflected in the difference in the reduction peak. Fluoride doping modifies the local electronic structure, thereby influencing the reduction peak potential of Ti. This doping can fine-tune the voltage at which the $\text{Ti}^{4+}/\text{Ti}^{3+}$ reduction occurs, potentially leading to shifts in the reduction peak potential and enhanced cycling stability. Importantly, the higher reduction potential of NTPF in the 31 m KAc WIS electrolyte compared to the reported KTP (-1.3 V vs Ag/AgCl) effectively avoids hydrogen side reactions and improves electrochemical stability during cycling. The b -values, obtained from the oxidation and reduction peaks across different scan rates, were computed (as shown in Figure S13c,d, Supporting Information). In aqueous potassium-ion batteries (AKIBs), the diffusion-controlled contribution gradually decreases as the scan rate increases, ranging from 90% at 0.2 mV s^{-1} to 60% at 10 mV s^{-1} (Figure 5e). The typical voltage profile for capacitive current (shaded area) is contrasted with the total current at a scan rate of 2 mV s^{-1} (Figure S13e,f, Supporting Information). It is observable that the capacitive effect in NTP and NTPF

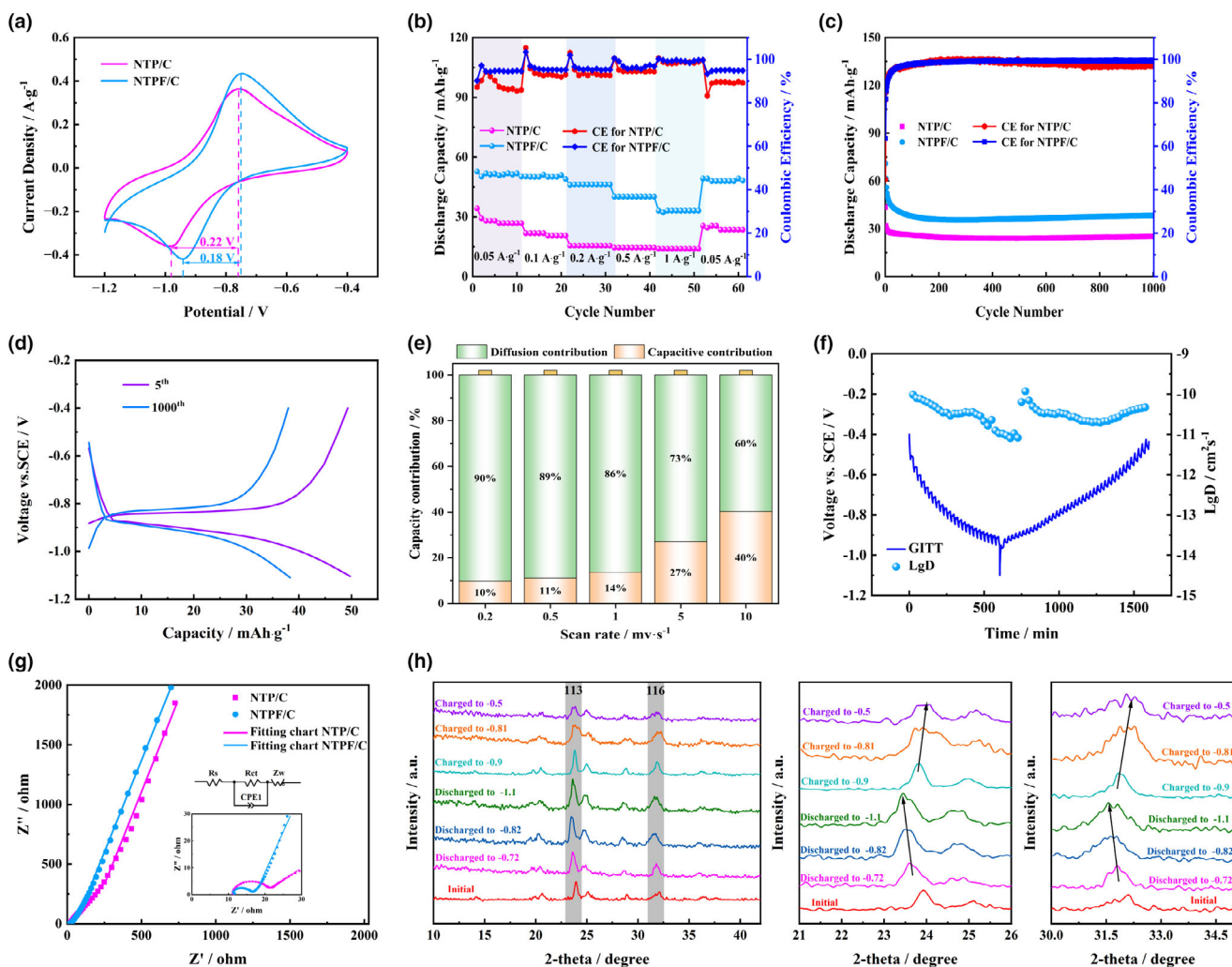


Figure 5. AKIBs 31 m KAC: a) Comparison of 2 mV s^{-1} for NTP/C and NTPF/C; b) Rate performance of NTP/C and NTPF/C composites; c) Cycling stability of NTP/C and NTPF/C composites; d) Charge/discharge curves of NTPF/C at a current density of 1 A g^{-1} ; e) Histogram of capacitance contribution; f) Voltage curves for the GITT test and the LgDK+ of NTPF/C; g) EIS of NTP/C and NTPF/C composites and equivalent circuit used for EIS fitting; h) Ex situ X-ray diffraction of NTPF/C electrode in AKIBs for initial, different discharge, and charge states.

accounts for 25.2% and 22%, respectively. The proportion in NTPF is slightly lower, possibly attributable to F doping, where K^+ tends to intercalate more within the lattice rather than being adsorbed onto the surface, thereby showcasing more distinct battery-type characteristics. The K^+ diffusion coefficients of NTP and NTPF materials were determined using GITT, as illustrated in Figure 4f and Figure S14, Supporting Information. In 31 M KAC WIS electrolyte, the K^+ diffusion coefficient of NTPF is $3.893 \times 10^{-11} \text{ cm}^2 \text{ s}^{-1}$, while for NTP is $4.868 \times 10^{-12} \text{ cm}^2 \text{ s}^{-1}$, indicating an enhancement in the potassium-ion diffusion coefficient of the NTPF anode electrode in AKIB following F doping.

Figure 5g illustrates the EIS profiles of NTP and NTPF, from which the interfacial impedance (R_{ct}), electrolyte impedance (R_s), and Warburg impedance (Z_w) were derived through fitting calculations (Table S4, Supporting Information). In the 31 m KAC WIS electrolyte, the EIS profiles indicated a higher R_s impedance compared to the corresponding R_s at lower salt concentrations of 5 M LiNO_3 and 5 M NaNO_3 ,

suggesting that the exceptionally high salt concentration sacrifices ion transfer rates in the aqueous electrolyte. Additionally, the smaller interfacial impedance (R_{ct}) and steeper slope in the low-frequency range of the NTPF electrode, relative to that of the NTP electrode, further suggest faster K^+ diffusion and transport during charging and discharging processes. We provide a comparative overview of representative doping strategies applied to NTP materials in aqueous alkali metal-ion batteries (Table S5, Supporting Information). Fluorine doping exhibits advantages in optimizing the electronic band structure and enhancing the electrochemical performance of NTP materials.

To further investigate the structural evolution of NTPF in the WIS AKIBs system, ex situ XRD measurements were conducted under various charging and discharging states. Figure 5h presents the XRD patterns of the NTPF electrodes at the initial stage and various discharging and charging stages after three cycles at 0.1 A g^{-1} . The characteristic diffraction peaks, such as (113) and (116), shift towards lower angles during K^+ insertion, indicating an expansion of the lattice structure.

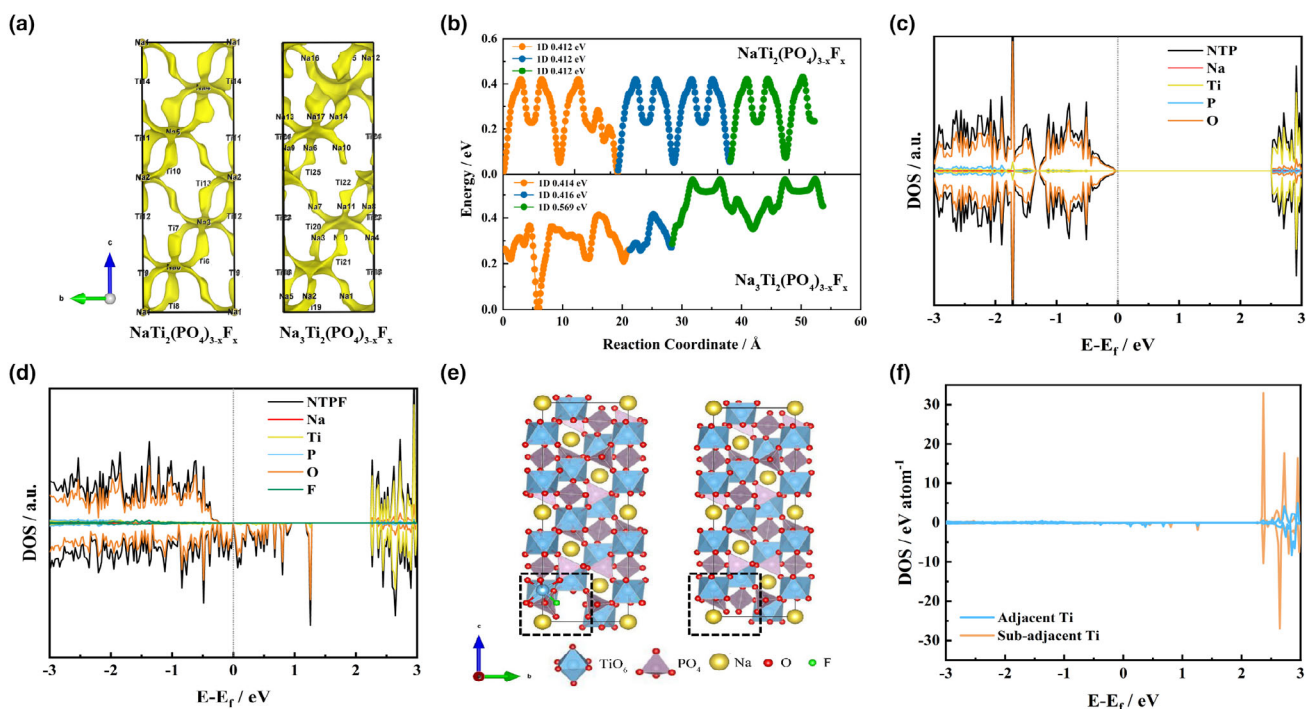
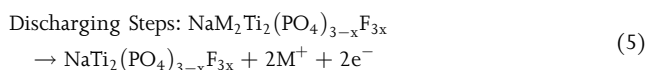
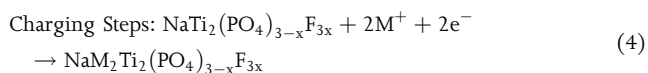


Figure 6. Bond valence site energy (BVSE) method of Na-ion migration within the NTPF structures: a) Naion migration pathways of $\text{NaTi}_2(\text{PO}_4)_{3-x}\text{F}_x$ and $\text{Na}_3\text{Ti}_2(\text{PO}_4)_{3-x}\text{F}_x$; b) Energy profiles of the migration pathways in $\text{NaTi}_2(\text{PO}_4)_{3-x}\text{F}_x$ and $\text{Na}_3\text{Ti}_2(\text{PO}_4)_{3-x}\text{F}_x$; Crystal structures and potential is surfaces are visualized using VESTA; DFT calculations: c, d) DOS for NTP and NTPF; e) Schematic diagram of the structure comparison between $\text{NaTi}_2(\text{PO}_4)_{3-x}\text{F}_x$ and $\text{NaTi}_2(\text{PO}_4)_3$; f) PDOS of Ti directly connected and interval connected with F in NTPF.

This shift is reversed during the extraction of K^+ ions, demonstrating a contraction of the lattice. The free energies of NTP, LTP, and KTP were obtained from theoretical calculations as -839.7 , -834.5 and -826.8 eV, respectively, indicating that NTP has the lowest energy and the most stable structure among the three structures, i.e., it is easier for Na^+ to occupy the M1 site compared to Li^+ and K^+ . The electrochemical reactions of NTPF in the three types of aqueous alkali metal-ion half cells are similar. Therefore, we summarize the reaction equation as follows, where M represents alkali metal ions (Li^+ , Na^+ and K^+).



2.5. Theoretical Calculations

To investigate the impact of F doping on the structural characteristics of NTP and its influence on ionic transport, the bond valence site energy (BVSE) method^[52] was utilized to analyze migration pathways and associated energy barriers. For the NTP structure, the most favorable migration pathway aligns with its NASICON-type open three-dimensional channel structure, allowing alkali metal ions to migrate along the path highlighted in yellow in Figure S15a, Supporting Information. The effective migration barrier is 0.398 eV. After fluorine ion doping, the ion migration path in the NTPF structure transitions from

a simple three-dimensional pathway to a multi-type migration channel, interconnecting one-dimensional, two-dimensional, and three-dimensional pathways (Figure 6a,b). Although the effective energy barrier remains largely unchanged before and after doping, the increased variety of channel types facilitates the rapid intercalation of alkali metal ions. In addition, during the charge and discharge process, the structures of two samples transform into $\text{Na}_3\text{Ti}_2(\text{PO}_4)_3$ and $\text{Na}_3\text{Ti}_2(\text{PO}_4)_{3-x}\text{F}_x$, respectively. Due to the insertion of sodium ions, the effective barrier is significantly increased, as depicted in Figure 6b and Figure S15b,d, Supporting Information. Both structures exhibit multiple types of ion migration channels (one-dimensional, two-dimensional, and three-dimensional). The incorporation of fluorine ions into the lattice of sodium titanium phosphate leads to changes in its lattice parameters and induces local distortions. These distortions affect the positioning and arrangement of titanium ions within the lattice. In NTP materials with open framework structures, doping of fluorine ions creates pathways that facilitate the movement of alkali metal ions, which is crucial for achieving high-rate capability and faster charge/discharge cycles.

To identify the oxidation states of Na, Ti, P, and O, a density of states (DOS) analysis was conducted (Figure 6c,d). The DOS profiles for both NTP and NTPF revealed similar characteristics, with the valence band primarily composed of O 2p states and the conduction band dominated by empty Ti 3d states. The analysis showed a significant reduction in the band gap. Narrowing the band gap could facilitate electron transfer between Ti ions with other ions. The band structure analysis corroborates these findings (Figure S16, Supporting Information). The NASICON-type NTP structure contains two distinct anion

sites. The two types of O sites are marked with different colors (red and green) in Figure S17, Supporting Information. The oxygen atoms at the red sites possess lower energy values compared to those at the green sites, indicating higher thermodynamic stability.^[27] Consequently, the oxygen atoms at the green sites are more likely to be replaced by F during doping. Based on the work of Wei et al.^[29] and Zhang et al.,^[30] F doping substitutes phosphate groups and forms bonds with Ti atoms in the TiO₆ octahedrons. The structural modifications introduced by F doping, along with the proposed bonding configurations, are displayed in Figure 6e. In the theoretical model, fluorine doping was introduced by substituting one of the 72 oxygen atoms in the NTP unit cell with a fluorine atom, in accordance with the atomic ratio obtained from the experimental XPS analysis.

The impact of fluorine doping was further examined, revealing a notable reduction in the band gap of phosphorus atoms (Figure S18, Supporting Information). In addition, the partial density of states (PDOS) of Ti directly connected with fluorine exhibits a weaker intensity compared to Ti that is interval bridged through the fluorine (Figure 6f and Figure S19, Supporting Information). This alteration facilitates more excess electrons hopping to sub-adjacent Ti atoms. The overlap of PDOS between adjacent and sub-adjacent Ti to O in NTP allows charge to hop to interval Ti_{2g} orbitals more effectively than to sub-adjacent Ti_{2g}, which in turn facilitates alkali metal ions insertion and extraction.

3. Conclusion

This study investigates the electrochemical properties and reaction kinetics of F-doped NaTi₂(PO₄)₃ as an electrode material for Li-, Na-, and K-ion batteries. XPS, XANES analysis, and DFT calculations reveal that F substitution alters the electronic energy levels and the localized electronic structure of Ti atoms. EIS tests and BVSE method studies reveal that F doping within the NTP structure reduces the diffusion resistance of alkali metal ions, lowers the ion diffusion energy barrier, and facilitates the formation of more favorable migration pathways. Electrochemical performance tests show that doping with F elements amplifies the reversible capacity and cycling stability of NTPF materials. Through systematic investigation, NTP, traditionally employed in aqueous sodium-ion batteries, was extended to aqueous dilute lithium-ion electrolytes and high-concentration potassium-ion electrolytes, demonstrating advancements in the enhancement of the NTP anode for aqueous alkali metal-ion batteries.

4. Experimental Section

Detailed information related to the synthesis of active electrodes, physicochemical characterization, and electrochemical evaluation of bifunctional electrodes towards UOR and supercapacitor application is provided in Supporting Information.

Acknowledgements

This work is supported by the National Natural Science Foundation of China (52072298, 51802261, 11675129), the Natural Science Basic Research Plan in Shaanxi Province of China (2025JC-YBQN-758), Scientific Research Program Funded by Shaanxi Provincial Education Department (Program No. 23JK0662), and the Youth Innovation Team of Shaanxi Universities.

Conflict of Interest

The authors declare no conflict of interest.

Supporting Information

Supporting Information is available from the Wiley Online Library or from the author.

Keywords

aqueous Li/Na/K-ion batteries, electronic structure, ionic conductivity, NASICON-type NaTi₂(PO₄)₃ electrode

Received: April 1, 2025

Revised: April 20, 2025

Published online: May 6, 2025

- [1] X. H. Yuan, F. X. Ma, L. Q. Zuo, J. Wang, N. F. Yu, Y. H. Chen, Y. S. Zhu, Q. H. Huang, R. Holze, Y. P. Wu, T. van Ree, *Electrochem. Energy Rev.* **2021**, DOI: [10.1002/s41918-020-00075-2](https://doi.org/10.1002/s41918-020-00075-2).
- [2] H. Y. Wang, M. M. Liang, Z. C. Miao, *Chem. Eng. J.* **2023**, 470, 144148.
- [3] H. Y. Wang, M. M. Liang, P. F. Yang, Z. C. Miao, *Chem. Eng. J.* **2024**, 495, 153530.
- [4] M. H. Lee, S. J. Kim, D. Chang, J. Kim, S. Moon, K. Oh, K. Y. Park, W. M. Seong, H. Park, G. Kwon, B. Lee, K. Kang, *Mater. Today* **2019**, 29, 26.
- [5] L. Zhu, M. M. Wang, S. Xiang, L. Fu, D. Sun, X. B. Huang, Y. X. Li, Y. G. Tang, Q. Zhang, H. Y. Wang, *ACS Nano* **2024**, 18, 13073.
- [6] B. Patra, R. Hegde, A. Natarajan, D. Deb, D. Sachdeva, N. Ravishankar, K. Kumar, G. S. Gautam, P. Senguttuvan, *Adv. Energy Mater.* **2024**, 14, 2304091.
- [7] M. Li, C. Sun, X. Y. Yuan, Y. Li, Y. F. Yuan, H. B. Jin, J. Lu, Y. J. Zhao, *Adv. Funct. Mater.* **2024**, 34, 2314019.
- [8] T. Bashir, S. Zhou, S. Yang, A. Ismail Sara, T. Ali, H. Wang, J. Zhao, L. Gao, *Electrochem. Energy Rev.* **2023**, DOI: [10.1002/s41918-022-00174-2](https://doi.org/10.1002/s41918-022-00174-2).
- [9] M. M. Liang, Z. Y. Li, Y. X. Kang, X. L. Zhao, X. Z. Zhang, H. M. Zhang, H. Y. Wang, Z. C. Miao, C. Fu, *J. Mater. Chem. A* **2024**, 12, 4623.
- [10] J. Y. Wang, T. J. He, X. C. Yang, Z. J. Cai, Y. Wang, V. Lacivita, H. Kim, B. Ouyang, G. Ceder, *Nat. Commun.* **2023**, 14, 5210.
- [11] R. Thirupathi, V. Kumari, S. Chakrabarty, S. Omar, *Prog. Mater. Sci.* **2023**, 137, 101128.
- [12] G. Pleckaityte, M. Petruleviciene, L. Staisiunas, D. Tediashvili, J. Pilipavičius, J. Juodkazyte, L. Vilciauskas, *J. Mater. Chem. A* **2021**, 9, 12670.
- [13] Y. H. Man, J. L. Sun, X. W. Zhao, L. P. Duan, Y. T. Fei, J. C. Bao, X. Y. Mo, X. S. Zhou, *J. Colloid Interface Sci.* **2023**, 635, 417.
- [14] Z. Tang, S. Zhou, Y. Huang, H. Wang, R. Zhang, Q. Wang, D. Sun, Y. Tang, H. Wang, *Electrochem. Energy Rev.* **2023**, DOI: [10.1002/s41918-022-00178-y](https://doi.org/10.1002/s41918-022-00178-y).
- [15] Z. X. Liu, Y. F. An, G. Pang, S. Y. Dong, C. Y. Xu, C. H. Mi, X. G. Zhang, *Chem. Eng. J.* **2018**, 353, 814.
- [16] Z. Jiang, Y. H. Li, C. Han, X. W. Wu, Z. X. He, J. Zhu, W. Meng, L. Dai, L. Wang, *Ceram. Int.* **2020**, 46, 4402.
- [17] K. Wang, Y. Liu, X. T. Xu, Y. Jiao, L. K. Pan, *Chem. Eng. J.* **2023**, 463, 142394.
- [18] W. L. Liao, T. F. Hung, M. M. Abdelaal, C. H. Chao, C. C. Fang, S. G. Mohamed, C. C. Yang, *J. Energy Storage* **2022**, 55, 105719.
- [19] B. Ding, M. Z. Li, F. Z. Zheng, Y. Z. Ma, G. S. Song, X. L. Guan, Y. Cao, C. E. Wen, *Batteries-Basel* **2023**, 9, 265.
- [20] B. He, K. B. Yin, W. B. Gong, Y. W. Xiong, Q. C. Zhang, J. Yang, Z. X. Wang, Z. Wang, M. X. Chen, P. Man, P. Coquet, Y. G. Yao, L. T. Sun, L. Wei, *Nano Energy* **2021**, 82, 105764.

- [21] L. Fu, X. Xue, Y. G. Tang, D. Sun, H. L. Xie, H. Y. Wang, *Electrochim. Acta* **2018**, 289, 21.
- [22] B. D. Zhao, Q. Y. Wang, S. Zhang, C. Deng, *J. Mater. Chem. A* **2015**, 3, 12089.
- [23] B. D. Zhao, B. Lin, S. Zhang, C. Deng, *Nanoscale* **2015**, 7, 18552.
- [24] X. J. Shen, Y. C. Xiong, F. Yu, J. Ma, *J. Mater. Chem. A* **2023**, 11, 17263.
- [25] G. Gece, J. Pilipavicius, N. Traskina, A. Drabavicius, L. Vilciauskas, *ACS Sustain. Chem. Eng.* **2023**, 11, 3429.
- [26] Z. G. Hou, X. Q. Zhang, J. W. Chen, Y. T. Qian, L. F. Chen, P. S. Lee, *Adv. Energy Mater.* **2022**, 12, 2104053.
- [27] Q. C. Wang, S. He, H. Chen, Z. Q. Peng, Z. X. Xu, Z. Y. Zeng, C. Wang, P. Xue, L. B. Ni, X. G. Li, J. Han, *Green Chem.* **2024**, 26, 2114.
- [28] Q. Deng, Q. Cheng, X. Z. Liu, C. D. Chen, Q. H. Huang, J. Li, W. T. Zhong, Y. J. Li, J. H. Hu, H. Wang, L. J. Wu, C. H. Yang, *Chem. Eng. J.* **2022**, 430, 132710.
- [29] P. Wei, Y. X. Liu, Y. R. Su, L. Miao, Y. Y. Huang, Y. Liu, Y. G. Qiu, Y. Y. Li, X. Y. Zhang, Y. Xu, X. P. Sun, C. Fang, Q. Li, J. T. Han, Y. H. Huang, *ACS Appl. Mater. Interfaces* **2019**, 11, 3116.
- [30] X. Zhang, H. X. Chen, H. Chen, S. L. Li, Y. R. Zhang, Y. H. Zheng, *J. Alloys Compd.* **2021**, 885, 161007.
- [31] J. T. Wu, L. X. Yang, H. J. Liu, H. P. Bu, W. J. Wang, C. L. Zeng, S. L. Zhu, *J. Appl. Electrochem.* **2022**, 52, 1563.
- [32] X. K. He, Q. T. Zou, L. Y. Wu, *J. Alloys Compd.* **2021**, 859, 157836.
- [33] J. J. Gu, S. J. Zhang, X. Y. Zhang, C. Y. Li, A. H. Wu, Q. H. Li, W. T. Mao, K. Y. Bao, *J. Solid State Electrochem.* **2023**, 28, 2093.
- [34] W. G. Zheng, M. Wu, C. Yang, Z. G. Tang, H. N. Hu, *Ceram. Int.* **2020**, 46, 12921.
- [35] F. Zhang, W. F. Li, X. D. Xiang, M. L. Sun, *Chem.-Eur. J.* **2017**, 23, 12944.
- [36] C. Y. Wu, S. C. Huang, J. Patra, C. C. Lin, C. S. Ni, J. K. Chang, H. Y. Chen, C. Z. Lu, *MRS Energy Sustain.* **2022**, 9, 350.
- [37] X. J. Liu, Z. F. Li, X. H. Zhong, C. X. Wang, S. Dmytro, *Ionics* **2024**, 30, 1437.
- [38] H. Wang, H. Zhang, Y. Cheng, K. Feng, X. Li, H. Zhang, *J. Mater. Chem. A* **2017**, 5, 593.
- [39] M. R. Wang, G. X. Liu, H. Q. Wang, H. Z. Zhang, X. F. Li, H. M. Zhang, *J. Mater. Chem. A* **2018**, 6, 7639.
- [40] A. Venkatesha, D. Seth, R. M. Varma, S. Das, M. Agarwal, M. A. Haider, A. J. Bhattacharyya, *ChemElectroChem* **2023**, 10, e202201013.
- [41] J. Pilipavicius, N. Traskina, J. Juodkazyte, L. Vilciauskas, *Electrochim. Acta* **2023**, 465, 142993.
- [42] Y. T. He, H. Q. Chen, Y. J. Wang, Y. M. Zhang, L. R. Hou, R. Y. Jiang, C. Z. Yuan, *Electrochim. Acta* **2023**, 447, 142128.
- [43] L. Chen, J. Y. Liu, Z. W. Guo, Y. G. Wang, C. X. Wang, Y. Y. Xia, *J. Electrochem. Soc.* **2016**, 163, A904.
- [44] D. P. Leonard, Z. X. Wei, G. Chen, F. Du, X. L. Ji, *ACS Energy Lett.* **2018**, 3, 373.
- [45] J. H. Sun, L. H. Xiao, S. D. Jiang, G. X. Li, Y. Huang, J. X. Geng, *Chem. Mater.* **2015**, 27, 4594.
- [46] X. F. Wang, Z. J. Feng, X. L. Hou, L. L. Liu, M. He, X. S. He, J. T. Huang, Z. H. Wen, *Chem. Eng. J.* **2020**, 379, 122371.
- [47] Z. Y. Han, S. Y. Zhao, J. W. Xiao, X. W. Zhong, J. Z. Sheng, W. Lv, Q. F. Zhang, G. M. Zhou, H. M. Cheng, *Adv. Mater.* **2021**, 33, 2105947.
- [48] J. Kim, S. Park, S. Hwang, W. S. Yoon, *J. Electrochem. Sci. Technol.* **2022**, 13, 19.
- [49] T. Xu, M. S. Zhao, Z. Su, W. Y. Duan, Y. Z. Shi, Z. Li, V. G. Pol, X. P. Song, *J. Power Sources* **2021**, 481, 229110.
- [50] H. El-Shinawi, J. Janek, *RSC Adv.* **2015**, 5, 14887.
- [51] D. Lan, X. Qu, Y. Tang, L. Liu, J. Liu, *J. Electrochem.* **2022**, 28, 2102231.
- [52] K. Wang, Q. Y. Ren, Z. Q. Gu, C. M. Duan, J. Z. Wang, F. Zhu, Y. Y. Fu, J. P. Hao, J. F. Zhu, L. H. He, C. W. Wang, Y. Y. Lu, J. Ma, C. Ma, *Nat. Commun.* **2021**, 12, 4410.